

Unsupervised 3D Keypoint Estimation with Multi-View Geometry

Sina Honari, Pascal Fua
Computer Vision Lab, EPFL, Switzerland

Abstract

Given enough annotated training data, 3D human pose estimation models can achieve high accuracy. However, annotations are not always available, especially for people performing unusual activities. In this paper, we propose an algorithm that learns to detect 3D keypoints on human bodies from multiple-views without any supervision other than the constraints multiple-view geometry provides. To ensure that the estimated 3D keypoints are meaningful, they are re-projected to each view to estimate the person’s mask that the model itself has initially estimated. Our approach outperforms other state-of-the-art unsupervised 3D human pose estimation methods on the Human3.6M and MPI-INF-3DHP benchmark datasets.

1. Introduction

Supervised 3D human pose estimation methods have become very effective [18, 31, 45] when enough annotated training data is available. However, this is not always the case since labeling images requires considerable effort, time, and financial resources. Hence, there has been growing interest in self-supervised methods [1, 2, 10, 11, 13, 32]. One way to address this is to learn unsupervised keypoints, distinct from pose labels, whose location and correlation is learned without any supervision by the model. The learned keypoints can later be mapped to the target pose of interest such as joint locations. On this line of research some self-supervised methods learn to find 2D keypoints [20, 21, 28, 35, 37, 38, 42, 44] but do not propose a way to extend them to 3D.

In this work, we aim to learn in a completely unsupervised fashion to extract 3D keypoints in multi-view image setups, such as the one depicted by Fig. 1. We assume the cameras to be calibrated and have access to an estimate of the background image of the scene but do not require 2D annotations, 3D annotations, or pre-trained models. Some approaches [3, 30, 36] also extract unsupervised 3D keypoints from input images. However, they have only been demonstrated on toy datasets with controllable dynamics and limited variations. By contrast, we aim at large datasets, fea-

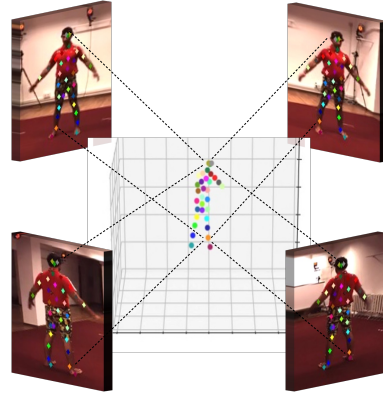


Figure 1. Multi-View Geometry for Unsupervised 3D Keypoint Estimation. Our approach predicts unsupervised 2D keypoints in each view and then uses multi-view geometry to construct 3D keypoints. These keypoints (observed above), whose location is learned without any supervision, can be later mapped to the final pose of interest (e.g. the joint locations).

turing people performing different activities.

In this paper, we propose a framework that first extracts unsupervised 2D points from individual images acquired by the cameras. These 2D detections are triangulated into potential 3D keypoints. Knowing it is easy to learn the foreground subject’s mask given an estimate of the background image, we use it to train a network that predicts the foreground subject’s mask. The potential 3D keypoints are then re-projected into each view to reconstruct this target mask that captures the subject’s posture. Our complete pipeline is depicted by Figure 2. This framework guarantees that the 3D keypoints satisfy multi-view projection properties while correlating strongly with the actual 3D pose of the subject. The 3D keypoints can then easily be mapped to the target 3D pose using a simple linear or multi-layer perceptron network.

In short, we propose a real-world unsupervised 3D keypoints estimation method that can be applied directly to uncurated images, without using any pre-trained pipelines, labels, or feature extractors. We show that our approach outperforms state-of-the-art unsupervised learning methods on Human3.6M and MPI-INF-3DHP benchmark datasets.

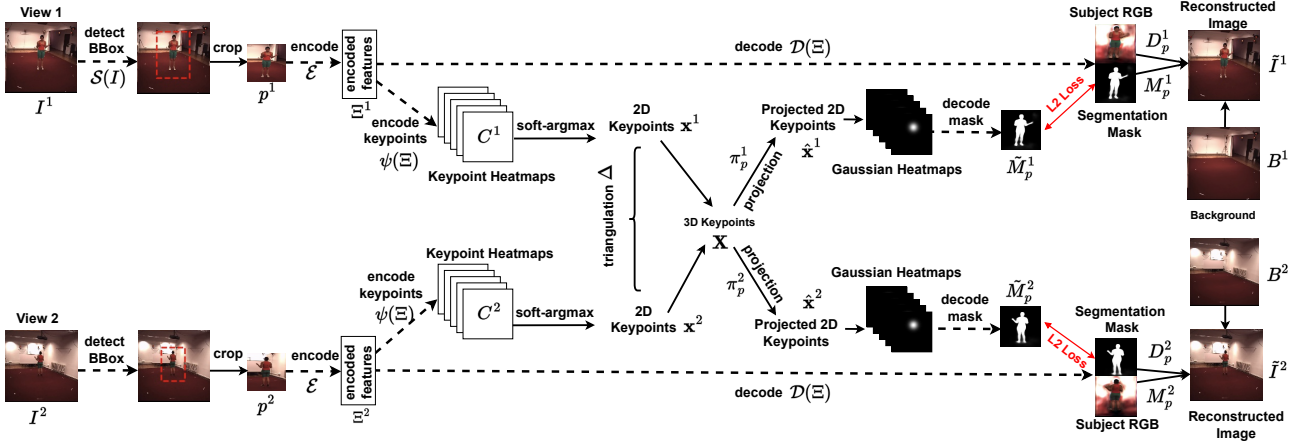


Figure 2. Approach. Given images from different views and an estimate of the background image, the model first detects and crops the subject in each view. The cropped patch is then passed to an encoder that encodes only the foreground subject information Ξ through reconstruction of the input image by prediction of the foreground mask M_p . This constitutes the image-reconstruction path. The encoded features Ξ are then used to detect 2D keypoints x by applying soft-argmax to each keypoint channel. The 2D keypoints from different views are then triangulated to obtain 3D keypoints X in the world-coordinate using full camera projection matrices, which are then projected separately to each view to obtain the view-specific 2D keypoints \hat{x} . These 2D keypoints are then used to construct a mask \tilde{M}_p by minimizing its difference to the mask M_p predicted by the model itself in the image-reconstruction path. No label is used for detection or mask reconstruction. The dashed line indicate trainable models.

2. Related Work

The objective of unsupervised learning models [1, 2, 10, 11, 13, 32] is to pre-train neural networks or extract distilled information from input images without relying on labels. The quality of the extracted features is then evaluated on the downstream application using a simple model, such as linear adaptation [1, 2, 10, 11], or a two hidden layer multi-layer perceptron (MLP) [13, 32, 33] among others. In this section, we briefly review unsupervised models for keypoint detection and pose estimation.

Unsupervised 2D keypoint models. There have been multiple approaches [20, 21, 28, 35, 37, 38, 42, 44] that propose unsupervised 2D keypoint estimation. However, the extension of these models to 3D keypoint estimation has not been explored. Moreover, these methods usually rely on center-cropped subject images, while our approach can directly work on uncurated images.

Unsupervised 3D pose estimation. On the other hand, some approaches learn unsupervised 3D poses from 2D using cross-views re-projection and matching [6, 17, 24, 27, 34, 41], temporal consistency [15, 39, 43] or through consistency across single frame lifting, rotation, and projection by learning a prior over the 2D pose distribution [4, 40]. However, all of these approaches rely on either 2D labels or pre-trained 2D pose estimation models, which still depend on considerable amount of annotations. In this paper, we aim at finding unsupervised keypoints directly from images, without relying on any labels or pre-trained models.

Unsupervised pose-relevant feature extraction. Simi-

lar to our approach, the works in [7, 13, 32, 33] apply unsupervised learning directly on input images to extract pose-relevant information. In particular, the approaches in [7, 13] apply temporal learning to extract time-variant information, while the approaches in [32, 33] leverage multi-view geometry by applying latent features rotation from one view to another. These latent features cannot be visualized as keypoints, as they live in uninterpretable latent layers that are mapped to images through complex decoders. Contrary to these approaches, we apply a full-projection matrix including both intrinsics and the translation component of the extrinsics. This allows directly projecting the estimated 3D keypoints back to the images using complete projection matrices, which contributes to further structure into the latent space, hence yielding interpretable 3D keypoints that correlate strongly with the subject’s pose. In practice, this intrinsic structure contributes to higher pose accuracy.

Kundu *et al.* [25, 26] also propose unsupervised 3D pose estimation models through pose and shape disentanglement and a spatial transformation map [26] or a part-based body model [25]. The proposed framework requires a very complex design and training procedure. Our experimental results show that we can achieve higher accuracy without resorting to such extra complexity.

Unsupervised 3D keypoint models. Some approaches extract unsupervised 3D keypoints from 3D point clouds [5, 8] or a 3D shape [22]. Contrary to these approaches, we aim at extracting unsupervised 3D keypoints from only input images. On the other hand, the approaches in [3, 30, 36]

learn 3D keypoints from input images using a multi-view learning framework. In particular, Chen *et al.* [3] learn latent 3D keypoints for control in reinforcement-learning problems. Noguchi *et al.* [30] estimate keypoint by applying a volumetric rendering using signed-distance-functions to reconstruct all views. This creates a complex setup that requires at least 5 cameras for training. Our model, on the other hand is much simpler to train, with fewer loss terms, and can even train with 2 cameras.

Closest to our approach is [36], which learns unsupervised 3D keypoints on rigid objects. While this approach also leverages multi-view geometry, similar to [3, 30] it has been only evaluated on toy datasets, with the possibility of rendering many views and limited diversity in appearance, pose and depth values. As we will show later, this approach is prone to limitations when dealing with real-world data. Moreover, none of these approaches handle foreground subject extraction, as they use toy datasets with no or simple backgrounds, with [30, 36] requiring ground-truth masks.

3. Method

Our goal is to train a network in an unsupervised fashion to find 3D keypoints in multi-view calibrated images. To ensure the keypoints are meaningful, we need to guarantee they encode information about only the foreground subject rather than about the background. To this end, the model should first detect the subject and then encode the foreground information. This is achieved by reconstructing the input image through prediction of a mask that separates foreground from background, hence allowing to encode only the foreground information.

Our network first encodes the foreground subject and uses the resulting image features to predict 2D keypoints in each view. The 2D keypoints from different views are then triangulated using calibration data to create 3D keypoints expressed in world-coordinates. These 3D keypoints are the features of interest in our model. Without any backward loop, there is no guarantee that they are meaningful. Hence, they are re-projected to each view to obtain 2D view-dependent keypoints, which are then passed to a mask decoder that reconstructs the foreground subject mask. This process is depicted in Figure 2. In the following sections, we describe the pipeline components in more details.

3.1. View-Dependent Feature Extraction

In this section, we describe how detection, encoding, and decoding components are used to extract view-dependent information and the foreground mask. Given an input image \mathbf{I} , a spatial transformer network (STN) [19] \mathcal{S} is used to extract four parameters; two of which specify the scale s^x, s^y and the other two the center of the bounding box u^x, u^y , yielding $\mathcal{S}(\mathbf{I}) = (s^x, s^y, u^x, u^y)$. A patch \mathbf{p} is then cropped

using the bounding box coordinates and is then passed to an encoder \mathcal{E} yielding $\mathcal{E}(\mathbf{p}) = \Xi$.

A decoder \mathcal{D} then takes the encoded features and outputs an RGB image patch $\tilde{\mathbf{D}}_{\mathbf{p}}$ together with a foreground mask patch $\mathbf{M}_{\mathbf{p}}$, which can be written as

$$\mathcal{D}(\Xi) = (\mathbf{D}_{\mathbf{p}}, \mathbf{M}_{\mathbf{p}}). \quad (1)$$

Finally, the inverse operation of the spatial transformer network (STN) is applied to put the patches back into the full-image resolution, yielding $\mathcal{S}^{-1}(\mathbf{D}_{\mathbf{p}}, \mathbf{M}_{\mathbf{p}}) = (\mathbf{D}, \mathbf{M})$. Decoded image \mathbf{D} is then merged with the background image \mathbf{B}^1 , using the predicted mask \mathbf{M} to reconstruct the input image $\tilde{\mathbf{I}}$. This operation is equal to

$$\tilde{\mathbf{I}} = \mathbf{M} \times \mathbf{D} + (1 - \mathbf{M}) \times \mathbf{B}, \quad (2)$$

where \times indicates the Hadamard product. This process is depicted in Figure 2. The input image reconstruction is crucial to capture information only about the foreground subject into the latent features in addition to estimating the foreground subject mask. Note that all of the components including foreground subject detection and mask prediction are unsupervised. They are all trained through input image reconstruction.

3.2. Unsupervised 3D Keypoint Estimation

The latent information in each view $\Xi^{\vartheta}, \vartheta \in \{1, \dots, V\}$, with V being the total number of views, is passed to a 2D keypoint encoder ψ that outputs N channels, one for each estimated keypoint n . This yields

$$\psi(\Xi) = \{C_n : n = 1, \dots, N\}, \quad (3)$$

where we refer to the set of $\{C_n\}_{n=1}^N$ by C . A soft-argmax operation [14] is then applied to each channel C_n to obtain a 2D keypoint $\mathbf{x}_n = (u, v)_n$. This can be written as

$$\begin{bmatrix} u_n \\ v_n \end{bmatrix} = \sum_{i,j} \text{softmax}(C_n)_{i,j} \begin{bmatrix} i \\ j \end{bmatrix}, \quad (4)$$

where the standard softmax operation is applied to each channel C_n to obtain a probability distribution, with i, j indicating the row and column coordinates of the channel. In summary, this process obtains a weighted-average of the coordinates, where the weights are given by the softmax probability map.

Given an intrinsic matrix $\mathbf{K}_{\mathbf{I}}$ specifying the projection from the camera coordinates to the pixel coordinates on image \mathbf{I} and an extrinsic matrix \mathbf{E} giving the change of coordinate system from camera to world coordinates, the camera projection matrix on the full image resolution can be written as $\mathbf{\Pi}_{\mathbf{I}} = \mathbf{K}_{\mathbf{I}}\mathbf{E}$.

¹The background image is obtained by taking per-pixel median of every frame in the video sequence.

Having the scale parameter (s^x, s^y) and the top-left coordinates (b^x, b^y) of the bounding box estimated by the spatial transformer network \mathcal{S} , the intrinsic matrix of the full-resolution image

$$\mathbf{K}_I = \begin{bmatrix} f^x & 0 & c^x \\ 0 & f^y & c^y \\ 0 & 0 & 1 \end{bmatrix} \quad (5)$$

is updated to correspond to the detected patch \mathbf{p} by using

$$\mathbf{K}_p = \begin{bmatrix} s^x f^x & 0 & s^x(c^x - b^x) \\ 0 & s^y f^y & s^y(c^y - b^y) \\ 0 & 0 & 1 \end{bmatrix}. \quad (6)$$

This yields the updated projection matrix of the detected patch $\mathbf{\Pi}_p = \mathbf{K}_p \mathbf{E}$.

For each keypoint $n \in \{1, \dots, N\}$, its corresponding 2D locations $\{\mathbf{x}_n^\vartheta\}_{\vartheta=1}^V$ and projection matrices $\{\mathbf{\Pi}_p^\vartheta\}_{\vartheta=1}^V$ from all V views are then passed to a triangulation operation Δ to output potential 3D keypoint $\mathbf{X}_n = (x, y, z)_n$ by

$$\Delta(\{\mathbf{x}_n^\vartheta\}_{\vartheta=1}^V, \{\mathbf{\Pi}_p^\vartheta\}_{\vartheta=1}^V) = \mathbf{X}_n. \quad (7)$$

We use direct linear transform [9] for triangulation, which is differentiable and allows back-propagation through the keypoints. Note that this triangulation operation is applied separately for each keypoint. The semantic consistency of the keypoints is enforced through multi-view geometry, as the n -th keypoint from different views are mapped together.

The potential keypoints $\{\mathbf{X}_n\}_{n=1}^N$ are the feature of interest that we will eventually use from the network’s prediction. The obtained keypoints so far are not guaranteed to contain any useful information as they are unsupervised. We use the foreground subject mask to constrain the keypoints in order to make them correspond to the subject. To do so, each 3D keypoint \mathbf{X}_n is first re-projected to each view by using $\mathbf{\Pi}_p$, this yields

$$\hat{\mathbf{x}}_n = (\hat{u}, \hat{v})_n = \mathbf{\Pi}_p(\mathbf{X}_n). \quad (8)$$

The set of re-projected 2D keypoints $\{\hat{\mathbf{x}}_n\}_{n=1}^N$ in each view is then passed to a mask-decoder ϕ that estimates the mask of the foreground subject $\tilde{\mathbf{M}}_p$, which is equivalent to

$$\tilde{\mathbf{M}}_p = \phi(\{\hat{\mathbf{x}}_n\}_{n=1}^N). \quad (9)$$

This creates a full pipeline validating the obtained 3D keypoints correspond to the foreground subject and satisfy the multi-view constraints. Note that the semantic of each keypoint is learned automatically by the model through this process.

3.3. Unsupervised Training Losses

Here we elaborate the losses used to train the unsupervised keypoint extraction model.

Image Reconstruction Loss. The reconstructed image $\tilde{\mathbf{I}}$, described in Section 3.1, should match to the input image \mathbf{I} using two losses; an RGB pixel-wise loss, and a perceptual loss using ImageNet features [13,23,32]; comparing the extracted features of the first 3 layers of the ResNet18 [12]. This can be written as

$$\mathcal{L}_{\text{reconst}} = \|\mathbf{I} - \tilde{\mathbf{I}}\|_2^2 + \beta \sum_{l=1}^3 \|\text{Res}_l(\mathbf{I}) - \text{Res}_l(\tilde{\mathbf{I}})\|_2^2. \quad (10)$$

Mask Reconstruction Loss. The estimated mask patch \mathbf{M}_p in the image-reconstruction module of Section 3.1, is taken as target for the mask $\tilde{\mathbf{M}}_p$ predicted from keypoints in Section 3.2 to minimize

$$\mathcal{L}_{\text{mask}} = \|\tilde{\mathbf{M}}_p - \mathbf{M}_p\|_2^2. \quad (11)$$

In order to further enforce the predicted keypoints lie in the foreground mask \mathbf{M}_p and enhance the location of the detected bounding box, the two following losses are also used.

Coverage Loss. Each projected keypoint $\hat{\mathbf{x}}_n$ should be only on the foreground subject mask \mathbf{M}_p and not the background. To enforce this, a Gaussian heatmap \mathbf{H} is first generated by taking its mean to be the keypoint $\hat{\mathbf{x}}_n$ ². This map is then normalized to have a probability map that sums to one, which equals to

$$\mathbf{H}_{\text{norm}} = \mathbf{H} / \sum_{i,j} (\mathbf{H}_{i,j}). \quad (12)$$

The coverage loss in Eq. (13) then maximizes the linear projection of \mathbf{H}_{norm} onto \mathbf{M}_p . This ensures the probability mass in \mathbf{H}_{norm} falls into locations of the mask \mathbf{M}_p that correspond to the foreground subject. This can be written as

$$\mathcal{L}_{\text{coverage}} = |1 - \mathbf{H}_{\text{norm}} \odot \mathbf{M}_p|, \quad (13)$$

where \odot indicates the dot product.

Bounding Box Centering Loss. To ensure the bounding box completely covers the foreground subject, we enforce the center of the predicted keypoints on the subject to be equal to the center of the detected bounding box. This loss together with $\mathcal{L}_{\text{reconst}}$ of Eq. (10) force the predicted bounding box to completely cover the keypoints and hence the detected subject.

Considering $\mathbf{u} = (u^x, u^y)$ to be the center of the predicted bounding box, as described in Section 3.1, and the

²its standard deviation was set to a fixed small value, $\sigma = 0.02$ in our experiments.

set of re-predicted keypoints on the subject to be $\{\hat{\mathbf{x}}_n\}_{n=1}^N$, the loss then equals to

$$\mathcal{L}_{\text{centering}} = \left| \mathbf{u} - \sum_{n=1}^N \hat{\mathbf{x}}_n \right|. \quad (14)$$

The total loss for training the model is then equal to

$$\mathcal{L}_{\text{unsup}} = \mathcal{L}_{\text{reconst}} + \gamma \mathcal{L}_{\text{mask}} + \delta \mathcal{L}_{\text{coverage}} + \eta \mathcal{L}_{\text{centering}}. \quad (15)$$

3.4. Pose Estimation

Once the unsupervised model is trained, 3D keypoints are extracted using the procedure explained in Section 3.2. To verify the quality of the learned unsupervised 3D keypoints $\mathbf{X} = \{\mathbf{X}_n\}_{n=1}^N$, we map them to the pose labels $\mathbf{Y} = \{\mathbf{Y}_m\}_{m=1}^M$, specifying body-joint locations, using a simple linear or two hidden-layer multi-layer perceptron (MLP) θ by minimizing

$$\mathcal{L}_{\text{pose}} = \|\theta(\mathbf{X}) - \mathbf{Y}\|_2^2. \quad (16)$$

Note that the pose labels are only used to evaluate the quality of the predicted unsupervised 3D keypoints through this mapping. They are not used for training the 3D keypoint model.

4. Experiments

In this section, we first present the evaluation datasets and metrics. Then, we compare our model quantitatively with other unsupervised approaches. Finally, we present ablation studies.

4.1. Datasets

We use the following 3D human pose benchmark datasets.

Human3.6M [16] (H36M). As in [13, 32], we use subjects 1, 5, 6, 7, and 8 to train the unsupervised keypoint estimation model. This yields 308,760 training samples. Subjects 9 and 11 are used for evaluation, sub-sampled every 10 frames, applied uniformly over video frames. This yields 53,720 test images. We show qualitative results of the estimated unsupervised 2D and 3D keypoints in Fig. 3.

MPI-INF-3DHP [29] (3DHP). We use subjects 1 to 6 for training and subjects 7 and 8 for evaluation. We take only frames where the person is the foreground subject³. This yields 59,952 frames for training and 7,312 frames for evaluation. We show qualitative results of the unsupervised keypoint predictions in Fig. 4.

³We leave out frames with the actor on a chair as this occludes the foreground subject.

4.2. Comparison to the State-of-The-Art Models

The qualitative results of Figs. 3 and 4 indicate that our approach captures 3D pose effectively, as the keypoints remain consistent across views. To quantify this, we compare against other unsupervised 3D and 2D approaches as well as to a pre-trained ImageNet feature extractor. We report 3D pose errors using mean per joint position error (MPJPE), the normalized N-MPJPE, and the procrustes aligned P-MPJPE between predicted and ground-truth 3D poses.

Table 1. Comparison with 3D approaches on H36M (in mm).

Approach	Model	MPJPE	N-MPJPE	P-MPJPE
Unsupervised	KeypointNet [36]	158.7	156.8	112.9
	NVS [33]	-	115.0	-
	Kundu <i>et al.</i> [25]	99.2	-	-
	Kundu <i>et al.</i> [26]	-	-	89.4
	Temporal Contrastive [13]	100.3	99.3	74.9
	Ours	73.8	72.6	63.0

Table 2. Comparison with 3D models on 3DHP (in cm).

Approach	Model	MPJPE	N-MPJPE	P-MPJPE
Unsupervised	DrNet [7]	22.28	21.55	14.94
	NSD [32]	20.24	19.29	14.09
	Temporal Contrastive [13]	20.95	19.78	14.04
	Ours	14.57	14.21	11.52

Unsupervised 3D Approaches. We compare against state-of-the-art unsupervised approaches on the H36M dataset in Table 1 and on the 3DHP dataset in Table 2. We outperform the competing methods discussed in Section 2.

Table 3. Comparison with 2D keypoint estimation models. All models predict 32 keypoints on 6 actions of wait, pose, greet, direct, discuss, and walk and regress a linear model from 2D keypoints to the 2D pose labels.

Model	%-MSE Error
Thewlis <i>et al.</i> [37]	7.51
Zhang <i>et al.</i> [44]	4.14
Schmidke <i>et al.</i> [35]	3.31
Lorenz <i>et al.</i> [28]	2.79
Jakab <i>et al.</i> [21]	2.73
Ours	2.38

Unsupervised 2D models For completeness, even though our primary goal is to compute 3D keypoints, we compare the predicted 2D keypoints \mathbf{x}_n of Eq. (4) with those produced by other unsupervised 2D approaches. Table 3 shows that we also outperform these approaches.

Supervised Pre-Training. As in recent unsupervised papers [1, 10, 11, 13], we compare the quality of our unsupervised keypoints to the features obtained by a fully-supervised ImageNet model. This evaluation highlights how much the extracted features by these models are suitable for the downstream application, which in the case of

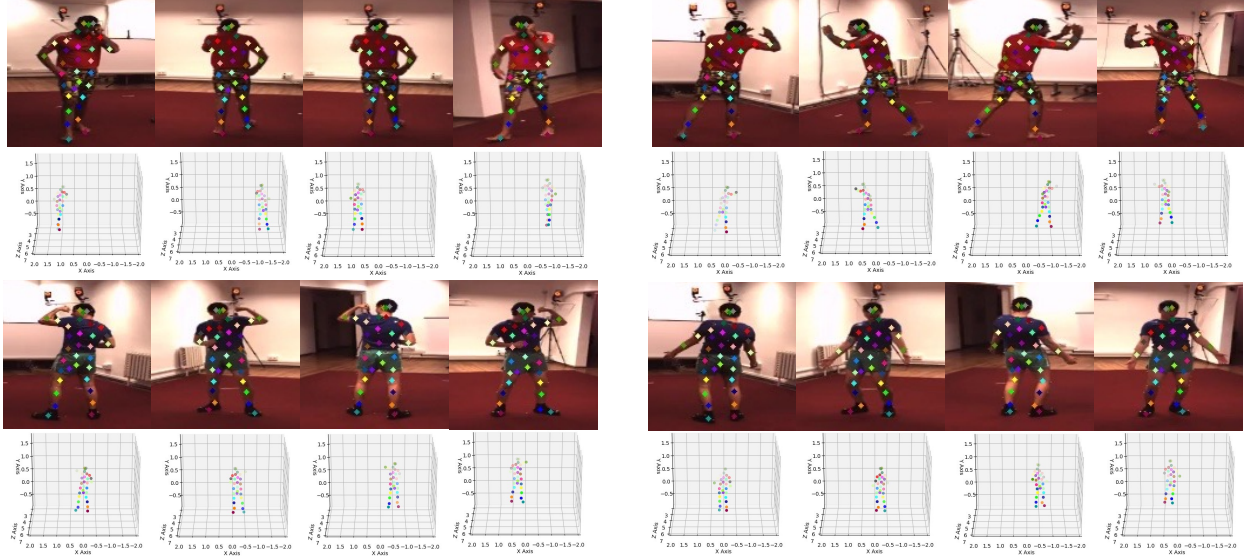


Figure 3. 2D and 3D keypoints found by a 32-keypoint prediction model on H36M. The 2D keypoints are consistent across views and the 3D keypoints capture the pose of the person, which indicates that they correlate well with the person’s posture.

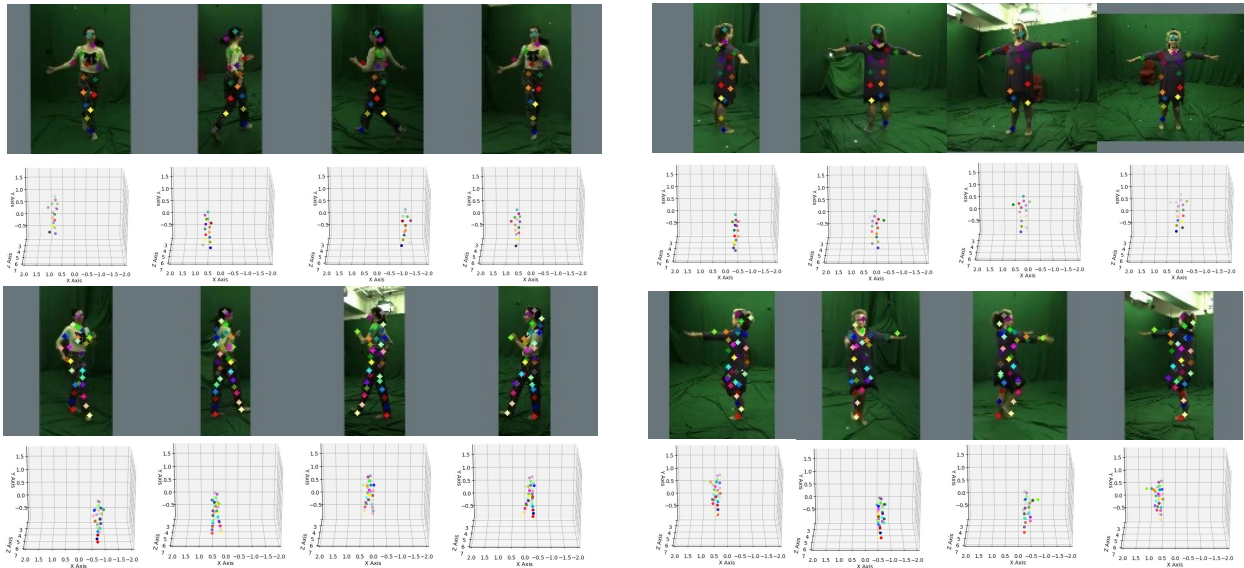


Figure 4. 2D and 3D keypoints found by 16- (top row) and 32- (bottom row) keypoint prediction models on 3DHP. As in Fig. 3, the 2D keypoints are consistent across views and the 3D keypoints capture the pose of the person.

this paper is 3D human pose estimation. The results are shown in Figure 5. The gap in MPJPE is over 75 mm in all cases, with our approach reducing the error by about 50% in the fully-supervised case. This indicates the impact of the proposed keypoint extraction approach and the structure that it learns into the latent 3D keypoints.

4.3. Ablation Studies

In this section we evaluate the impact of different loss and model components.

4.3.1 Contribution of the Loss Components

We first study the contribution of each loss component in Eq. (15). The results are presented in Table 4. The first row only reconstructs the input image using Eq. (10) without any 3D keypoint estimation. In this case the latent features Ξ are mapped to the 3D poses, as they are the closest latent representation to the pose. As observed in Table 4, this case has about 37 mm (corresponding to 50%) higher MPJPE error compared to our best approach in the last line.

The second row adds the mask reconstruction loss of

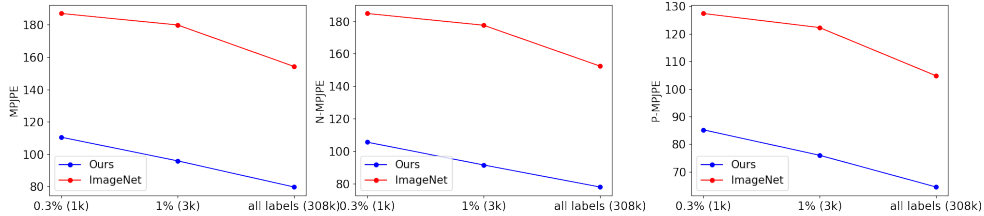


Figure 5. Comparison against the latent features of the pre-trained ImageNet model on H36M using the ResNet50 architecture [12]. The three plots from left to right show depict MPJPE, NMPJPE, and PMPJPE (in mm) for different percentage of labeled 3D data. Both models use a 2-hidden layer MLP to regress either the 3D keypoints (Ours) or the latent features—features before the classification layer in ImageNet—to the target 3D pose.

Eq. (11). This improves the results by about 32 mm compared to the first row indicating the structure of the latent 3D keypoints has a considerable impact. In the third and fourth rows, we respectively add the coverage loss of Eq. (13) and the centering loss of Eq. (14), where the last row shows our final model with all the features activated. While these losses have a relatively small contribution, by making a total improvement of about 8%, they still help improving the accuracy. This further indicates that these two losses can be removed without hurting much the accuracy to further simplify the approach.

Table 4. Ablation Study on Losses. Each column shows the impact of adding a loss term in Eq. (15) in the unsupervised learning phase. The last row shows our model with all features activated. All models use a 2-hidden layer MLP to map the latent features or the unsupervised keypoints to the 3D pose labels. The results are presented in millimeters (mm) on H36M dataset, with a lower value indicating a lower error.

$\mathcal{L}_{reconst}$	\mathcal{L}_{mask}	$\mathcal{L}_{coverage}$	$\mathcal{L}_{centering}$	MPJPE	N-MPJPE	P-MPJPE
✓	✗	✗	✗	111.8	107.6	79.7
✓	✓	✗	✗	79.9	78.6	67.0
✓	✓	✓	✗	78.3	77.0	65.6
✓	✓	✓	✓	73.8	72.6	63.0

4.3.2 Keypoint, Label and Pose-Model Complexity

In this section we study how much the size and complexity of some important model variables affects the results, in addition to showing the impact of the number of labelled data. One key question is how many unsupervised keypoints does the model need to predict and how does this hyper-parameter impact the results? Figure 6 shows the results for 3 different numbers of keypoints:

- 17: equal to the number of labelled 3D joints on the H36M dataset.
- 32: a number in-between the two bounds.
- 200: the number of keypoints to match prior

works [13, 32]⁴.

As observed in Figure 6, increasing the number of latent keypoints increases the accuracy. However, the gap between 17 and 32 keypoints is bigger than the one between 32 and 200 keypoints. This indicates 32 can be a reasonable number of keypoints on H36M without adding much complexity.

The complexity of the pose estimator model indicates how far the estimated keypoints are from the labelled pose. The more the complexity of the required pose model, the more the keypoints lie in an unrelated latent space, which requires more complex adaptation to map them to the actual pose of the subject. Our results in Figure 6 show that while a simple 2-hidden layer MLP obtains more accurate results, a simpler linear adaptation of the keypoints to the pose labels can still obtain decent results. This further shows the robustness of the estimated unsupervised keypoints and indicates that it correlates strongly with the target pose.

In Table 5, we further evaluate the impact of the number of keypoints on 3DHP dataset. Similar to H36M dataset, higher accuracy is obtained with more keypoints. For this dataset, we found 48 keypoints to obtain decent accuracy without adding extra complexity. Hence, we use 48 keypoints in other evaluations done on this dataset.

Table 5. Evaluation on the number of keypoints in 3DHP dataset (in cm). All models use a 2-hidden layer MLP for the pose regressor model.

Number of keypoints	Pose Model	MPJPE	N-MPJPE	P-MPJPE
16	2-hid MLP	16.16	15.76	12.28
32	2-hid MLP	15.53	15.52	11.87
48	2-hid MLP	14.57	14.21	11.52
96	2-hid MLP	14.16	13.90	11.14

4.3.3 Number of Views

One of the features of our approach is using multi-view triangulation by aggregating predictions from different views.

⁴The dimensionality of the extracted latent features in these methods, which serves as the input dimensionality to the pose model, is 600, which equals to 200 3D keypoints.

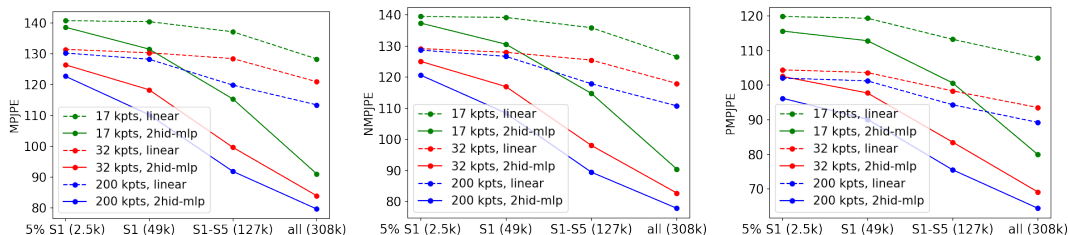


Figure 6. Analysis of the impact of the number of unsupervised keypoints, pose model complexity, and the amount of labelled data on H36M dataset. The three plots show results on MPJPE, NMPJPE, and PMPJPE (in mm). Each plot depicts the impact of trained models using 17, 32, and 200 unsupervised keypoints. For each model, two pose-regressors are trained; one using a linear model (the dashed line) and another using a 2-hidden layer MLP (the solid line). The X axes shows the percentage of 3D labels.

One question is how many views are required for a robust pose estimation? To answer this question we train different models with 2, 3, and 4 views. The results are reported in Table 6. As expected, higher accuracy is obtained with more views, since the triangulation obtains more robust 3D keypoints. However, 3 views is enough to obtain robust results, with a clear gap with 2 views and a small gap with 4 views.

Table 6. Evaluation on the number of views used for triangulation (in mm). In all cases 32 unsupervised 3D keypoints are predicted by the model. All models use a 2-hidden layer MLP for the pose regressor model. Results are reported on H36M dataset.

Number of Views	Pose Model	MPJPE	N-MPJPE	P-MPJPE
2	2-hid MLP	103.21	100.7	81.6
3	2-hid MLP	77.7	75.7	64.0
4	2-hid MLP	73.8	72.6	63.0

4.3.4 Target Mask

One feature of our network is that it reconstructs the mask that model has itself estimated in the image-reconstruction module. The quality of the obtained mask directly impacts the accuracy of the model as this is the target for the predicted keypoints. If one has access to ground-truth mask, how much the results would change? To answer this question we train two variants, one using the full pipeline of Section 3 with all elements of Eq. (15), and another by omitting $\mathcal{L}_{reconst}$ from it. Note that in the latter variant there is no image-reconstruction and the encoded features Ξ are used to only reconstruct the mask. The results are reported in Table 7. While both models obtain close results, our predicted mask obtains slightly better results than the ground-truth one, which indicates the robustness of our mask prediction.

We also compare with a case that a mask is obtained by background reduction from the input image and then normalizing it. This approach, however, leads to higher error, as we observed the color of the subject’s clothes can interfere with proper background reduction. The results indicate that while our approach does not need ground-truth masks,

its estimated mask captures better the foreground subject, which leads to higher accuracy.

Table 7. Impact of different target masks (in cm). In the first row a mask is obtained by reducing background from the input image and normalizing it in $[0, 1]$. In the 2nd row the ground-truth mask is used and in the final row our model’s predicted mask is used to train unsupervised keypoint model. All models predict 48 unsupervised 3D keypoints on the MPI dataset and use a 2-hidden layer MLP for the pose regressor model.

Mask Used	Pose Model	MPJPE	N-MPJPE	P-MPJPE
IMG - BG	2-hid MLP	17.48	16.93	12.64
Ground-truth	2-hid MLP	14.57	14.21	11.52
Predicted (Ours)	2-hid MLP	14.37	13.98	10.99

5. Conclusion and Limitations

In this paper we proposed an unsupervised technique that leverages the full projection properties of a multi-view system to predict 3D keypoints by reconstructing the foreground subject’s mask. In doing so, our model obtains keypoints that are consistent across different views and correspond to the foreground subject. We show its application on real-world data featuring articulating human bodies.

There are multiple directions that our approach can be improved. Our approach works on images with a single foreground subject. The existence of multiple foreground entities can occlude the mask, leading to extraction of keypoints that lie on all of them. Another limitation is the dependence of an estimation of the background image to help learning the mask of the foreground subject. While as we show in Section 4.3.4, our model does not need to rely on ground-truth masks and does a better job than background subtraction from the input image, it requires a background image in the pipeline. Moreover, our keypoints can jitter on consecutive frames of a video. Leveraging a temporal constraint can enhance the consistency of the obtained keypoints across time. Finally, our approach requires a multi-view setup, with at least two cameras for extraction of 3D keypoints. We leave these extension to future work.

References

- [1] H. Bao, L. Dong, S. Piao, and F. Wei. BEiT: BERT Pre-Training of Image Transformers. In *International Conference on Learning Representations*, 2022. 1, 2, 5
- [2] M. Caron, H. Touvron, I. Misra, H. Jégou, J. Mairal, P. Bojanowski, and A. Joulin. Emerging Properties in Self-Supervised Vision Transformers. In *International Conference on Computer Vision*, 2021. 1, 2
- [3] B. Chen, P. Abbeel, and D. Pathak. Unsupervised Learning of Visual 3D Keypoints for Control. In *ICML*, pages 1539–1549. PMLR, 2021. 1, 2, 3
- [4] C. Chen, A. Tyagi, A. Agrawal, D. Drover, R. MV, S. Stojanov, and J. M. Rehg. Unsupervised 3D Pose Estimation with Geometric Self-Supervision. In *Conference on Computer Vision and Pattern Recognition*, 2019. 2
- [5] N. Chen, L. Liu, Z. Cui, R. Chen, D. Ceylan, Ch. Tu, and W. Wang. Unsupervised learning of intrinsic structural representation points. In *CVPR*, pages 9121–9130, 2020. 2
- [6] X. Chen, K. Lin, W. Liu, C. Qian, and L. Lin. Weakly-Supervised Discovery of Geometry-Aware Representation for 3D Human Pose Estimation. In *Conference on Computer Vision and Pattern Recognition*, 2019. 2
- [7] Emily L Denton et al. Unsupervised Learning of Disentangled Representations from Video. In *Advances in Neural Information Processing Systems*, pages 4414–4423, 2017. 2, 5
- [8] C. Fernandez-Labrador, A. Chhatkuli, D. P. Paudel, J. J. Guerrero, C. Démonceaux, and L. V. Gool. Unsupervised learning of category-specific symmetric 3d keypoints from point sets. In *ECCV*, pages 546–563, 2020. 2
- [9] R. Hartley and A. Zisserman. *Multiple View Geometry in Computer Vision*. Cambridge University Press, 2000. 4
- [10] K. He, X. Chen, S. Xie, Y. Li, P. Dollár, and R. Girshick. Masked Autoencoders Are Scalable Vision Learners. In *Conference on Computer Vision and Pattern Recognition*, pages 16000–16009, 2022. 1, 2, 5
- [11] K. He, H. Fan, Y. Wu, S. Xie, and R. Girshick. Momentum Contrast for Unsupervised Visual Representation Learning. In *Conference on Computer Vision and Pattern Recognition*, pages 9729–9738, 2020. 1, 2, 5
- [12] K. He, X. Zhang, S. Ren, and J. Sun. Deep Residual Learning for Image Recognition. In *Conference on Computer Vision and Pattern Recognition*, pages 770–778, 2016. 4, 7, 1
- [13] S. Honari, V. Constantin, H. Rhodin, M. Salzmann, and P. Fua. Temporal Representation Learning on Monocular Videos for 3D Human Pose Estimation. *PAMI*, (01):1–12, 2022. 1, 2, 4, 5, 7
- [14] S. Honari, P. Molchanov, S. Tyree, P. Vincent, C. Pal, and J. Kautz. Improving Landmark Localization with Semi-Supervised Learning. In *Conference on Computer Vision and Pattern Recognition*, pages 1546–1555, 2018. 3
- [15] Xiaodan Hu and Narendra Ahuja. Unsupervised 3D Pose Estimation for Hierarchical Dance Video Recognition. In *ICCV*, pages 11015–11024, 2021. 2
- [16] C. Ionescu, I. Papava, V. Olaru, and C. Sminchisescu. Human3.6M: Large Scale Datasets and Predictive Methods for 3D Human Sensing in Natural Environments. *IEEE Transactions on Pattern Analysis and Machine Intelligence*, 2014. 5
- [17] U. Iqbal, P. Molchanov, and J. Kautz. Weakly-Supervised 3D Human Pose Learning via Multi-View Images in the Wild. In *Conference on Computer Vision and Pattern Recognition*, 2020. 2
- [18] K. Isakov, E. Burkov, V. Lempitsky, and Y. Malkov. Learnable Triangulation of Human Pose. In *International Conference on Computer Vision*, pages 7718–7727, 2019. 1
- [19] M. Jaderberg, K. Simonyan, A. Zisserman, and K. Kavukcuoglu. Spatial Transformer Networks. In *Advances in Neural Information Processing Systems*, pages 2017–2025, 2015. 3
- [20] T. Jakab, A. Gupta, H. Bilen, and A. Vedaldi. Unsupervised Learning of Object Landmarks through Conditional Image Generation. In *Advances in Neural Information Processing Systems*, 2018. 1, 2
- [21] T. Jakab, A. Gupta, H. Bilen, and A. Vedaldi. Self-Supervised Learning of Interpretable Keypoints from Unlabelled Videos. In *Conference on Computer Vision and Pattern Recognition*, pages 8787–8797, 2020. 1, 2, 5
- [22] T. Jakab, R. Tucker, A. Makadia, J. Wu, N. Snavely, and A. Kanazawa. Keypointformer: Unsupervised 3d keypoint discovery for shape control. In *CVPR*, pages 12783–12792, 2021. 2
- [23] J. Johnson, A. Alahi, and L. Fei-fei. Perceptual Losses for Real-Time Style Transfer and Super-Resolution. In *European Conference on Computer Vision*, pages 694–711, 2016. 4
- [24] M. Kocabas, S. Karagoz, and E. Akbas. Self-Supervised Learning of 3D Human Pose Using Multi-View Geometry. In *Conference on Computer Vision and Pattern Recognition*, 2019. 2
- [25] J. N. Kundu, S. Seth, V. Jampani, M. Rakesh, R. V. Babu, and A. Chakraborty. Self-Supervised 3D Human Pose Estimation via Part Guided Novel Image Synthesis. In *Conference on Computer Vision and Pattern Recognition*, 2020. 2, 5
- [26] J. N. Kundu, S. Seth, M.V. Rahul, M. Rakesh, R. V. Babu, and A. Chakraborty. Kinematic-Structure-Preserved Representation for Unsupervised 3D Human Pose Estimation. In *AAAI Conference on Artificial Intelligence*, volume 34, pages 11312–11319, 2020. 2, 5
- [27] Y. Li, K. Li, Sh. Jiang, Z. Zhang, C. Huang, and R. Xu. Geometry-Driven Self-Supervised Method for 3d Human Pose Estimation. In *AAAI*, volume 34, pages 11442–11449, 2020. 2
- [28] D. Lorenz, L. Bereska, T. Milbich, and B. Ommer. Unsupervised Part-Based Disentangling of Object Shape and Appearance. In *Conference on Computer Vision and Pattern Recognition*, pages 10955–10964, 2019. 1, 2, 5
- [29] D. Mehta, H. Rhodin, D. Casas, P. Fua, O. Sotnychenko, W. Xu, and C. Theobalt. Monocular 3D Human Pose Estimation in the Wild Using Improved CNN Supervision. In *International Conference on 3D Vision*, 2017. 5
- [30] A. Noguchi, U. Iqbal, J. Tremblay, T. Harada, and O. Gallo. Watch It Move: Unsupervised Discovery of 3D Joints for Re-

- Posing of Articulated Objects. In *CVPR*, pages 3677–3687, 2022. 1, 2, 3
- [31] E. Remelli, S. Han, S. Honari, P. Fua, and R. Wang. Lightweight Multi-View 3D Pose Estimation through Camera-Disentangled Representation. In *Conference on Computer Vision and Pattern Recognition*, 2020. 1
- [32] H. Rhodin, V. Constantin, I. Katircioglu, M. Salzmann, and P. Fua. Neural Scene Decomposition for Human Motion Capture. In *Conference on Computer Vision and Pattern Recognition*, 2019. 1, 2, 4, 5, 7
- [33] H. Rhodin, M. Salzmann, and P. Fua. Unsupervised Geometry-Aware Representation for 3D Human Pose Estimation. In *European Conference on Computer Vision*, 2018. 2, 5
- [34] H. Rhodin, J. Spoerri, I. Katircioglu, V. Constantin, F. Meyer, E. Moeller, M. Salzmann, and P. Fua. Learning Monocular 3D Human Pose Estimation from Multi-View Images. In *Conference on Computer Vision and Pattern Recognition*, 2018. 2
- [35] L. Schmidtke, A. Vlontzos, S. Ellershaw, A. Lukens, T. Arichi, and B. Kainz. Unsupervised Human Pose Estimation Through Transforming Shape Templates. In *CVPR*, pages 2484–2494, 2021. 1, 2, 5
- [36] S. Suwajanakorn, N. Snavely, J. Tompson, and M. Norouzi. Discovery of Latent 3D Keypoints via End-To-End Geometric Reasoning. In *Advances in Neural Information Processing Systems*, 2018. 1, 2, 3, 5
- [37] J. Thewlis, S. Albanie, H. Bilen, and A. Vedaldi. Unsupervised Learning of Landmarks by Descriptor Vector Exchange. In *International Conference on Computer Vision*, pages 6361–6371, 2019. 1, 2, 5
- [38] J. Thewlis, H. Bilen, and A. Vedaldi. Unsupervised Learning of Object Landmarks by Factorized Spatial Embeddings. In *International Conference on Computer Vision*, 2017. 1, 2
- [39] Sh. Tripathi, S. Ranade, A. Tyagi, and A. Agrawal. PoseNet3D: Learning Temporally Consistent 3D Human Pose via Knowledge Distillation. In *3DV*, pages 311–321, 2020. 2
- [40] B. Wandt, J. Little, and H. Rhodin. ElePose: Unsupervised 3D Human Pose Estimation by Predicting Camera Elevation and Learning Normalizing Flows on 2D Poses. In *CVPR*, pages 6635–6645, 2022. 2
- [41] B. Wandt, M. Rudolph, P. Zell, H. Rhodin, and B. Rosenhahn. Canonpose: Self-Supervised Monocular 3D Human Pose Estimation in the Wild. In *Conference on Computer Vision and Pattern Recognition*, 2021. 2
- [42] O. Wiles, A.S. Koepke, and A. Zisserman. Self-Supervised Learning of a Facial Attribute Embedding from Video. In *British Machine Vision Conference*, 2018. 1, 2
- [43] Z. Yu, B. Ni, J. Xu, J. Wang, Ch. Zhao, and W. Zhang. Towards Alleviating the Modeling Ambiguity of Unsupervised Monocular 3D Human Pose Estimation. In *ICCV*, pages 8651–8660, 2021. 2
- [44] Y. Zhang, Y. Guo, Y. Jin, Y. Luo, Z. He, and H. Lee. Unsupervised Discovery of Object Landmarks as Structural Representations. In *Conference on Computer Vision and Pattern Recognition*, pages 2694–2703, 2018. 1, 2, 5
- [45] Z. Zou and W. Tang. Modulated Graph Convolutional Network for 3D Human Pose Estimation. In *International Conference on Computer Vision*, 2021. 1

Unsupervised 3D Keypoint Estimation with Multi-View Geometry

— Supplementary Information

S.1. Model Architecture and Training

Unsupervised Model Architecture. The input image \mathbf{I} has a resolution of 500×500 pixels. The detector network \mathcal{S} takes the input image down-sampled by factor 4 and uses a ResNet18 [12] architecture to output 4 parameters (s^x, s^y, u^x, u^y) , two specifying the scale parameters (s^x, s^y) and two indicating the center of the bounding box (u^x, u^y) . These parameters are used to crop a patch \mathbf{p} from \mathbf{I} that is then resized to 128×128 . The encoder \mathcal{E} , which is a ResNet50 [12] architecture, then takes the patch \mathbf{p} and outputs a feature map Ξ of size 729 in H36M and 1029 in 3DHP dataset.

In the image reconstruction path, the decoder \mathbf{D} takes Ξ features and first applies a fully-connected layer with dropout and ReLU with an output size of 65,536 that is reshaped to 256×16^2 . These feature maps are then passed to three upsampling steps, with each step having one bilinear upsampling with factor 2 and followed by 3 convolutional layers. Each convolutional layer has a kernel size of 3×3 together with a ReLU non-linearity. These three upsampling steps change the feature maps from 256×16^2 respectively to 128×32^2 , 64×64^2 , and 32×128^2 . Finally, a convolutional layer with a kernel size of 1×1 maps the features from 32×128^2 to 4×128^2 dimension, where the first three channels of the output compose the RGB patch \mathbf{D}_p and the last channel yields the foreground subject mask \mathbf{M}_p .

In the unsupervised keypoints path, the features Ξ are passed to the keypoint encoder ψ , which is a network similar to the decoder \mathbf{D} (with distinct parameters) but with the difference that the final convolutional layer outputs features of size $N \times 128^2$, where each feature map $n \in \{1, \dots, N\}$ belongs to a different keypoint. Afterwards, the triangulation of 2D to 3D keypoints and re-projection from 3D keypoints to 2D keypoints in each view is applied as described in Section 3.2. These steps yield the re-projected keypoints $\{\hat{\mathbf{x}}_n\}_{n=1}^N$.

The mask decoder ϕ first builds a Gaussian heatmap of size 128×128 from each keypoint $\hat{\mathbf{x}}_n : n \in \{1, \dots, N\}$, where the center of the Gaussian blob in the heatmap n is the keypoint location $\hat{\mathbf{x}}_n = (\hat{u}, \hat{v})_n$ and its standard deviation is set to $\sigma = 0.02$. The set of N Gaussian heatmaps are then concatenated together, which creates a feature map of shape $N \times 128^2$. This feature map constitutes the Gaussian heatmaps of all keypoints on the foreground subject. The

mask decoder then applies on these features three convolutional layers each with a kernel size of 5×5 , a padding of 2×2 , and a stride of 1×1 . The first convolutional layer takes a feature map of size $N \times 128^2$ and outputs a feature map of size 1×128^2 , with the last two convolutional layers keeping the feature map at the same size. Mask decoder’s final output $\tilde{\mathbf{M}}_p$ hence has a shape of 1×128^2 , which can then be easily compared to the similarly sized mask \mathbf{M}_p . Figure 2 depicts the architecture.

Pose Model. To analyze the quality of the learned 3D keypoints, they are passed to either a linear or a 2-hidden layer MLP (depending on the evaluation setup in Section 4), where in the latter case each hidden layer has a dimensionality of 2048 followed by a ReLU and a 50% dropout. The output layer has a dimensionality of $3 \times M$, where M is 17 labelled joints in the H36M and 3DHP datasets.

Training Procedure. We train the unsupervised model’s parameters for 200K iterations with mini-batches of size 32 using an Adam optimizer, which takes about 2 days on a Tesla V100 GPU. We use a learning rate of $1e-4$ for all parameters, except the detector network \mathcal{S} and image decoder \mathbf{D} , which use $2e-5$. The pose model is also trained for 200K iterations using mini-batches of size 256 and a learning rate of $1e-4$, which takes few hours on the same GPU.

Regarding the hyper-parameters of Eq. (15), we set β to 2, δ to 0.01, η to 1.0, and γ respectively to 0.5 and 5.0 in the H36M and 3DHP datasets.

S.2. Qualitative Visualization

In figure S1 we show different target masks used for the experiments in Section 4.3.4. The second columns, which estimates the mask by reducing the background from the input image and normalizing it, obviously cannot capture a mask that separates background from the subject. This is due to the similarity of the clothes of the subject with the background materials that makes the distinction not trivial. We also tried thresholding this mask with different values, but there was no clear winning threshold, as different values either removed part of the subject or included the background, which indicates a mask cannot be easily obtained in such scenarios and further highlights the importance of the prediction of the mask by the model. In the third column the ground-truth mask provided by the dataset is depicted. As can be observed, this mask also cuts parts of the subject. Our predicted mask, on the other hand, can find the sub-

ject in an smooth and consistent way. The last row shows cases where the model also highlights the floor, which is due to the subject’s shadow in addition to the change of the floor covering that the model tries to capture. While these latter examples shows the model can capture small details, the mask regions other than the foreground subject can sometimes misguide some of the keypoints, since the keypoints try to reconstruct the mask. Nevertheless, our approach still yields cleaner masks compared to the other two variants, which contributes to better performance as shown in Table 7.

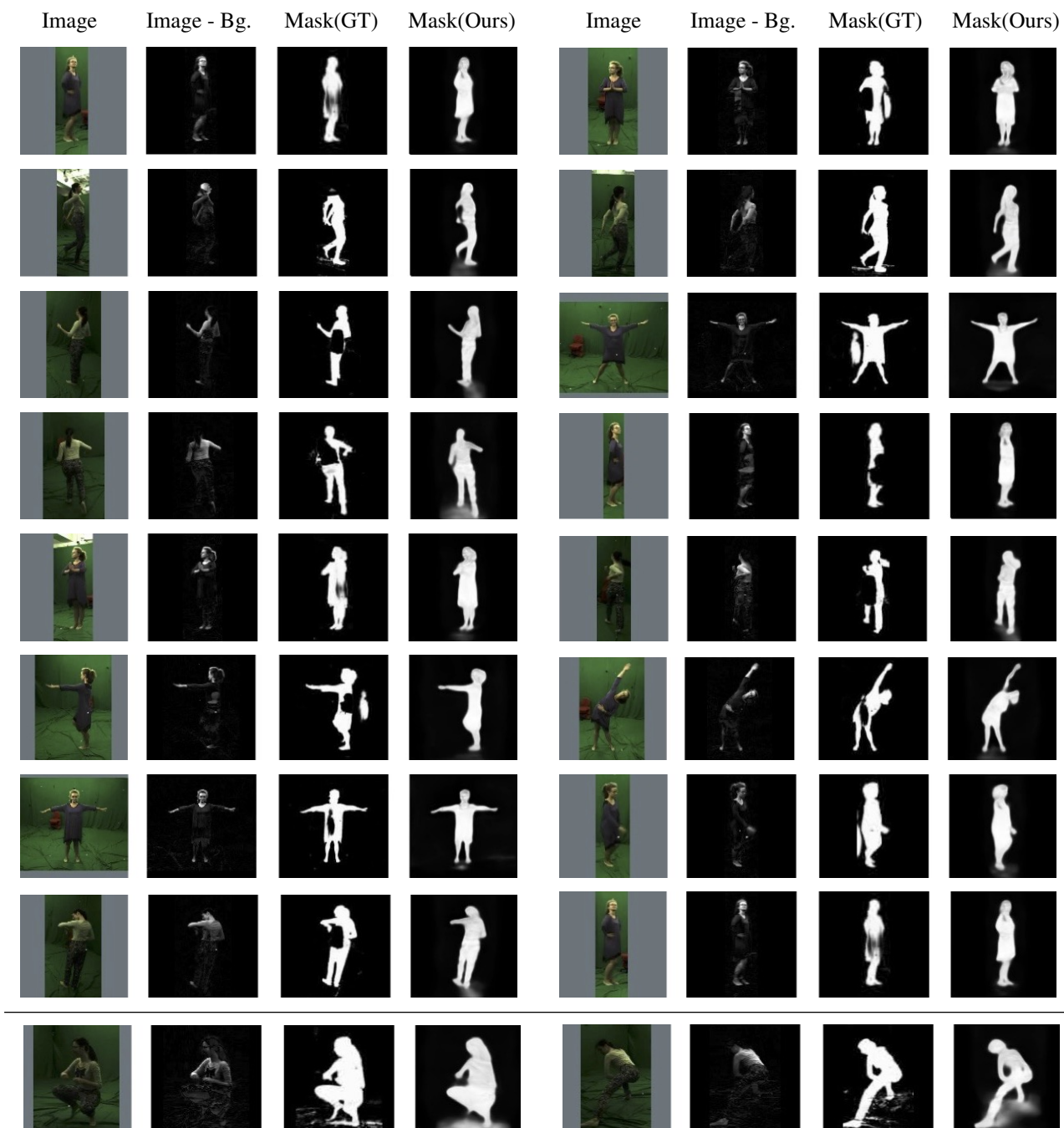


Figure S1. Different target masks. For each group of 4 consecutive pictures in a row, the first column shows the input image, the second column depicts the background reduced and normalized input image, the third and fourth columns respectively show the ground truth and the mask predicted by our model. The last row shows examples where our mask creates a noticeable highlight on the floor. This is due to the shadow of the person in addition to the movement of the floor covering that the model tries to capture.